

Lurking systematics in predicting galaxy cold gas masses using dust luminosities and star formation rates

Steven Janowiecki,^{1*} Luca Cortese,¹ Barbara Catinella,¹ Adelle J. Goodwin²

¹International Center for Radio Astronomy Research (ICRAR), M468, The University of Western Australia, 35 Stirling Highway, Crawley, WA, 6009, Australia

²School of Physics and Astronomy, Monash University, Clayton, Victoria, 3800, Australia

accepted version – 26 Jan 2018

ABSTRACT

We use galaxies from the *Herschel* Reference Survey to evaluate commonly used indirect predictors of cold gas masses. We calibrate predictions for cold neutral atomic and molecular gas using infrared dust emission and gas depletion time methods which are self-consistent and have $\sim 20\%$ accuracy (with the highest accuracy in the prediction of total cold gas mass). However, modest systematic residual dependences are found in all calibrations which depend on the partition between molecular and atomic gas, and can over/under-predict gas masses by up to 0.3 dex. As expected, dust-based estimates are best at predicting the total gas mass while depletion time-based estimates are only able to predict the (star-forming) molecular gas mass. Additionally, we advise caution when applying these predictions to high- z galaxies, as significant (0.5 dex or more) errors can arise when incorrect assumptions are made about the dominant gas phase. Any scaling relations derived using predicted gas masses may be more closely related to the calibrations used than to the actual galaxies observed.

Key words: Galaxies – galaxies: ISM – (ISM:) dust, extinction – radio lines: ISM

1 INTRODUCTION

Key to an understanding of galaxy evolution is a complete census of the baryonic components in galaxies: the stellar populations and the interstellar medium (ISM, gas and dust). These components are strongly connected to each other, mainly through the process of star formation. Atomic hydrogen gas (HI) is the raw fuel for star formation, but must first cool and condense into molecular hydrogen (H_2) before stars can form (e.g., Bigiel et al. 2008; Leroy et al. 2008, but see also Glover & Clark 2012). Once formed, stars eject gas and dust through stellar winds and also significantly pollute the ISM with enriched material.

The exquisite interplay between the multi-phase ISM and the star formation cycle has been observed in nearby galaxies in great detail. While star formation rates (SFRs) have been measured in large samples of galaxies for many decades (e.g., Roberts 1963; Kennicutt 1983; Alam et al. 2015), more recently several large observational programs have quantified galaxy ISM contents in a statistical way, including HI content (Catinella et al. 2010, 2013), H_2 content (Saintonge et al. 2011a), and dust content (da Cunha et al. 2010; Cortese et al. 2012). These studies and others have shown many connections between star formation and ISM

phases, including that H_2 is responsible for regulating galaxy SFRs (Tacconi et al. 2013; Saintonge et al. 2016), that the dust-to-gas mass ratio depends on metallicity (Draine et al. 2007; Leroy et al. 2011), and that the dust-to-stellar mass ratio depends on specific SFR (da Cunha et al. 2010).

Despite the abundance of high resolution and multi-wavelength observations of galaxies, our understanding of the gas-dust-star cycle is incomplete, even in the local Universe. Nonetheless, as observations of ISM components in galaxies at higher redshifts are becoming increasingly feasible, we are gaining new windows into galaxy evolution. However, the high redshift view is often limited or partial, and requires careful “calibration” when making comparisons with local galaxies.

Star formation rate is the most easily measured piece of the gas-dust-star cycle, and samples of star-forming galaxies have been observed out to high redshift (e.g., Whitaker et al. 2014; Alam et al. 2015). Extensive observations have consistently shown that the star formation history of the universe reaches a peak at $z \sim 2.5$ (Madau & Dickinson 2014), but direct observations of all ISM components are not yet as advanced (e.g., Carilli & Walter 2013). Observational challenges prevent the detection of 21cm HI emission in samples of galaxies beyond $z \sim 0.2$ (Catinella & Cortese 2015, but see recent detection at $z = 0.376$ from Fernández et al. 2016), but CO (a tracer of H_2) observations have begun slowly

* E-mail: steven.janowiecki@icrar.org (SJ)

reaching galaxies at higher redshifts (e.g., [Daddi et al. 2010](#); [Aravena et al. 2012](#); [Bauermeister et al. 2013](#); [Hodge et al. 2013](#); [Cybulski et al. 2016](#)).

Faced with the great difficulty (or impossibility) of directly observing the gaseous phases of galaxy ISM at high redshift, many observational campaigns have focused on *indirect* estimates of ISM masses. These estimators are based on correlations observed between properties of local galaxies, and are then applied at higher redshift.

These ISM mass predictions fall broadly into two categories: 1) mass-to-light ratios using far-infrared (FIR) luminosities or gas-to-dust ratios (e.g., [Magdis et al. 2012](#); [Eales et al. 2012](#); [Scoville et al. 2014](#)); and 2) starting from an integrated star formation law (e.g., the Kennicutt-Schmidt law (K-S); [Schmidt 1959](#); [Kennicutt 1998](#)) and inverting the observed SFR (i.e., a gas depletion time) to estimate a star-forming gas mass (e.g., [Tacconi et al. 2013](#); [Genzel et al. 2015](#); [Berta et al. 2016](#)). In the literature, these relations are typically calibrated with samples of local galaxies.

Recently, some groups have also explored the theoretical connections between simulated galaxies and different ISM mass predictions. [Goz et al. \(2017\)](#) use a fully cosmological hydrodynamical code to reproduce the multi-wavelength emission (ultraviolet to infrared) of galaxies, and validate some choices of indirect ISM mass indicators. Broadly, star formation can contribute to dust heating (making dust temperature a good tracer of SFR), but longer wavelength dust emission is tightly connected to gas masses.

A significant limitation in the development of these indirect relations is that each ISM mass component is usually calibrated independently with an observable quantity, which does not allow an analysis of possible systematic effects or residual dependencies on other ISM properties. For example, [Scoville et al. \(2014\)](#) use HI, CO, and FIR observations of a sample of 12 low- z spiral and starburst galaxies in order to calibrate a predictive relationship between FIR dust luminosity and total ISM mass (M_{ISM} , the sum of the HI, H₂, and dust components), but their sample is too small to test for secondary dependencies (e.g., on $M_{\text{HI}}/M_{\text{H}_2}$ ratio, SFR, etc). By contrast, [Scoville et al. \(2016\)](#) use the same dust luminosities to calibrate a prediction for molecular gas masses in a larger sample of 70 galaxies. This subtle shift requires an assumption about the relative contributions of HI, H₂, and dust to the total ISM mass. In a different work, the same FIR luminosities are used to instead predict total gas mass ($M_{\text{HI}} + M_{\text{H}_2}$) for 36 nearby galaxies ([Groves et al. 2015](#)).

While economical, these indirect estimates may suffer from unknown biases or systematic trends with other ISM properties of galaxies. Before using predicted gas masses to make conclusions about the evolution of high-redshift galaxies, we must first carefully examine these calibrations for any lurking systematic effects which could introduce variations as a function of galaxy properties and mask the true evolutionary trends.

We use a sample of galaxies with a *complete set of observations of all ISM components* to calibrate and test these predictive relations, in order to evaluate how internally consistent these estimators can be. We describe our local sample of galaxies and observations in Section 2. In Section 3 we use mass-to-light and gas-to-dust ratios to predict ISM masses, and Section 4 shows our calibrations using depletion times.

In Section 5 we compare these two types of calibrations with each other, and in Section 6 we discuss residual secondary dependences on other quantities. Section 7 includes a discussion of the scientific implications of these systematic effects, and in Section 8 we briefly summarize our main results. Throughout this work we assume a Λ CDM cosmology with $H_0=70 \text{ km s}^{-1} \text{ Mpc}^{-1}$, $\Omega_M=0.27$, and $\Omega_\Lambda=0.73$.

2 SAMPLE AND DATA

Our sample is selected from the *Herschel* Reference Survey (HRS), which was a volume-limited infrared (IR) imaging survey of 322 galaxies between 15 and 25 Mpc ([Boselli et al. 2010](#)). We select our Primary Sample (PS) of $N=68$ galaxies to be those HRS targets with a complete set of observations of the ISM components to calibrate and verify relationships between dust and gas content.

Required observations include detections in each of the *Herschel* bands (100-500 μm), detections of atomic and molecular gas (HI and CO), spectroscopic metallicity estimates, and reliable SFRs. Further, we select only galaxies which are not HI-deficient. The HI-deficiency parameter (Def_{HI}) is the logarithmic difference between the HI content expected based on a galaxy’s morphological type and optical diameter and its observed HI mass ([Haynes & Giovanelli 1984](#)). We require our PS sample to have $\text{Def}_{\text{HI}} \leq 0.5$ in order to exclude galaxies which have likely been stripped of their gas or otherwise affected by dense environments (e.g., [Cortese et al. 2016](#)). The 68 galaxies in our PS have been shown to be representative of a volume-limited sample, and do not suffer from significant selection effects (see Figure 1 in [Cortese et al. 2016](#)). We next briefly summarise each observed or derived quantity, their uncertainties, and the necessary assumptions. The uncertainties on each quantity typically reflect the errors associated with the measurement and not the calibration or systematic uncertainties, which may be even larger.

Stellar mass (M_) and distance (D):* M_* and D come from [Cortese et al. \(2012\)](#). Estimates of M_* are based on the colour-dependent mass-to-light ratios of [Zibetti et al. \(2009\)](#) and measured from Sloan Digital Sky Survey images ([Abazajian et al. 2009](#)). Uncertainties on M_* include only errors from the broadband flux measurements and not uncertainties from distances or mass-to-light ratios.

Star formation rate (SFR): We use SFRs from [Boselli et al. \(2015\)](#), who compiled and calibrated observations of star formation in the HRS. Specifically we use their “SFR_{MED}” which combines all available SFRs (including those from H α , FUV, 24 μm , and radio indicators). When available, uncertainties come from the errors on the H α fluxes or radio continuum fluxes; otherwise we adopt a 15% error as suggested in §5.1.1 of [Boselli et al. \(2015\)](#).

Metallicity ($12+\log(O/H)$): Spectroscopic gas-phase abundances come from [Hughes et al. \(2013\)](#), who observed HRS galaxies with drift-scan optical spectra and derived oxygen abundances using the calibrations of [Kewley & Ellison \(2008\)](#) to be consistent with the O3N2 scale of [Pettini & Pagel \(2004\)](#). When necessary, all metallicities used in this work (e.g., from [Leroy et al. \(2011\)](#); [Berta et al. \(2016\)](#) in Figure 1) are converted to the O3N2 scale ([Pettini & Pagel 2004](#)) via calibrations from [Kewley & Ellison \(2008\)](#). Uncer-

tainties are given by Hughes et al. (2013) and fully include the errors in converting to a common calibration of metallicity (see §3 of Hughes et al. 2013).

Monochromatic infrared luminosities: HRS IR data include imaging from the Photoconductor Array Camera and Spectrometer (PACS) and the Spectral and Photometric Imaging Receiver (SPIRE) instruments. PACS provided images at $100\mu\text{m}$ and $160\mu\text{m}$, and SPIRE at $250\mu\text{m}$, $350\mu\text{m}$, and $500\mu\text{m}$. Photometry based on these images was presented in Cortese et al. (2014) from PACS and in Ciesla et al. (2012) from SPIRE. We convert these flux measurements to luminosities in solar units (L_{\odot}). Uncertainties on the luminosities are propagated from published flux errors in Ciesla et al. (2012) and Cortese et al. (2014).

Dust mass (M_{dust}): We use the dust mass estimates (in M_{\odot}) from Ciesla et al. (2014). They fit spectral energy distributions (SEDs) between 8-500 μm using the dust models of Draine & Li (2007), and provide uncertainties on their mass estimates.

HI gas mass (M_{HI}): The atomic gas mass estimates come from Boselli et al. (2014), who compiled 21cm observations from the literature for HRS galaxies. When available, we propagate 21cm flux errors into M_{HI} uncertainties, otherwise we adopt the typical uncertainty of 15% errors on the mass (see §6 of Boselli et al. 2014).

Total gas mass (M_{gas}): Throughout this work we use the following definition of total gas mass: $M_{\text{gas}} = 1.36 \times (M_{\text{HI}} + M_{\text{H}_2})$. This includes a 36% correction for helium in the total gas mass (not included in M_{H_2} alone). Uncertainties are propagated from M_{HI} and M_{H_2} .

2.1 Molecular hydrogen masses (M_{H_2})

Estimates of molecular hydrogen gas mass come from the CO(1-0) observations and compilation of archival data in Boselli et al. (2014). They use a variable conversion factor between L_{CO} and M_{H_2} (X_{CO}) which depends on the near-IR luminosity (measured in the H filter) of each galaxy, following the calibration of Boselli et al. (2002), not including any contribution or correction from helium. Uncertainties on the mass are propagated from flux errors given in Boselli et al. (2014).

The variable X_{CO} from Boselli et al. (2002) relies on a number of assumptions. While a metallicity dependence is expected (Leroy et al. 2009), spectroscopic abundances were not available for all of the galaxies in the calibration sample. Instead, they demonstrated that a luminosity-dependent expression for X_{CO} works well for galaxies without metallicity measurements. Their total molecular gas masses also rely on the assumption that molecular clouds are virialized systems (see Section 4 of Bolatto et al. 2013 or McKee & Ostriker 2007 for further details).

As a simple way to consider the range of effects of different conversion methods, we include three alternative prescriptions for X_{CO} and briefly explore their effects on gas mass predictions. The first, $M_{\text{H}_2,c}$ is determined using the constant conversion factor from Galactic studies ($X_{\text{CO}} = 2.3 \times 10^{20} \text{ cm}^{-2} / (\text{K km s}^{-1})$, Strong et al. 1988). Second, we use the recent prescription of Accurso et al. (2017) which depends on metallicity and $sSFR$ to compute $M_{\text{H}_2,acc}$. Third, $M_{\text{H}_2,bol}$ comes from Bolatto et al. (2013) and depends on both metallicity and stellar surface den-

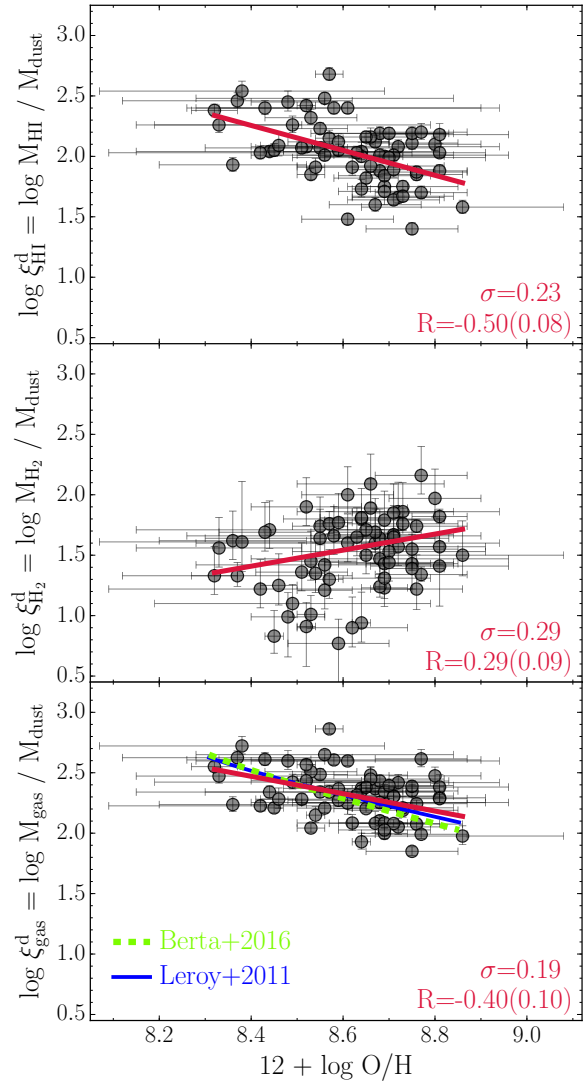


Figure 1. Calibration of ξ for each gas phase as a function of metallicity. Top: M_{HI} ; middle: M_{H_2} ; bottom: M_{gas} . Our best-fit relations are shown in red. The relations from Leroy et al. (2011) and Bert et al. (2016) are shown in blue and green, respectively, on the bottom panel. Best fit lines, Pearson’s correlation coefficient (R) and its uncertainty, and the standard deviations (σ , in dex) of points about the best-fit line are shown in red on each plot.

sity (determined from optical effective radius). While a full discussion of the relative advantages and disadvantages is outside the scope of this work, we re-derive our main calibrations using these alternatives as discussed in Section 4.3. Although the exact values of the relationships between dust luminosity and molecular gas mass change, these alternative prescriptions do not change the underlying systematic trends which are implicit in these relationships.

2.2 Gas-to-dust ratio (ξ) for each phase

The ratios of gas-to-dust mass are computed using each phase (HI, H₂, total). As this ratio varies with metallicity (Draine et al. 2007; Leroy et al. 2011), we explore the relationship between ξ ($M_{\text{dust}}/M_{\text{gas(phrase)}}$) and $12+\log(\text{O}/\text{H})$

for each phase. Figure 1 shows these relationships, with uncertainties shown as error bars. Note that the uncertainties on the metallicity are large, as they include both statistical and systematic errors associated with converting many observations to a common metallicity scale.

We estimate the uncertainty on Pearson’s R correlation coefficient, given in parentheses on Figure 1 and all subsequent, as the standard deviation of the R values of 10,000 random samples drawn from our data points. We allow for repeated values and require each randomly drawn sample to have the same total number of values as our real sample. As is the case throughout this work, red lines in Figure 1 show our best fits, which are found through least squares minimization of differences in the ordinate weighted by their uncertainties. These best-fitting relations are given below:

$$\begin{aligned}\log \xi_{\text{HI}}^{\text{d}} &= \log \frac{M_{\text{HI}}}{M_{\text{dust}}} = 10.92 \pm 2.00 - 1.03 \pm 0.23 \times (12 + \log \text{O}/\text{H}) \\ \log \xi_{\text{H}_2}^{\text{d}} &= \log \frac{M_{\text{H}_2}}{M_{\text{dust}}} = -4.17 \pm 2.23 + 0.67 \pm 0.26 \times (12 + \log \text{O}/\text{H}) \\ \log \xi_{\text{tot}}^{\text{d}} &= \log \frac{M_{\text{tot}}}{M_{\text{dust}}} = 8.51 \pm 1.65 - 0.72 \pm 0.19 \times (12 + \log \text{O}/\text{H}).\end{aligned}$$

Note that the relationship between $\xi_{\text{tot}}^{\text{d}}$ and $12 + \log \text{O}/\text{H}$ is the tightest (smallest scatter, σ , about the best-fit line) and also agrees with the relations of Leroy et al. (2011) and Berta et al. (2016). The relationship with $\xi_{\text{HI}}^{\text{d}}$ is the strongest (greatest absolute value of Pearson’s correlation coefficient, R), owing to the fact that our galaxies are HI-dominated (like most in the local universe). The relationship is very poor for M_{H_2} , where the correlation is actually the inverse of physical expectations (e.g., Leroy et al. 2011) and the scatter becomes even larger.

3 GAS MASS ESTIMATES FROM L_{IR} & M_{dust}

We start by considering the simplest possible correlations between cold gas masses (atomic, molecular, and total) and monochromatic IR luminosities, as shown in the first five columns of Figure 2. We also consider correlations with dust mass, with and without the metallicity-dependent ξ , as shown in the last two columns. In all cases we carry out least squares fitting weighted by the uncertainties from both axes. The minimization is only done for differences in the ordinate as these relationships are intended for use as predictions between “known” IR luminosities or dust masses and “unknown” ISM phase masses.

We caution against the blind application of these equations to diverse populations of galaxies. As will be shown in the following sections, calibrations of cold gas mass predictions are susceptible to a number of biases and systematic residual dependences on other physical properties. The best-fit predictions we derive from our sample may not be appropriate to use across all types of galaxies. Further discussions of these biases and their effects are included in Sections 6 and 7.

3.1 M_{HI} estimates from dust

Across the M/L estimates of M_{HI} , the strength and scatter improve continuously with increasing wavelength such that the best monochromatic predictor is L_{500} . Not only does L_{500} have a value of $R=0.75 \pm 0.05$ which is statistically larger than the next best value at $R=0.70 \pm 0.06$, but it also

has a scatter which is $\sim 8\%$ better than the next best. This is expected, as L_{500} is most closely connected to emission from the diffuse ISM. Multiplying M_{dust} by the metallicity-dependent $\xi_{\text{HI}}^{\text{d}}$ gives an even better prediction of M_{HI} , both in terms of R and σ . Our best three relationships are given below, where $\xi_{\text{HI}}^{\text{d}}$ was determined in Section 2.

$$\begin{aligned}\log \frac{M_{\text{HI}}}{M_{\odot}} &= 0.72 \pm 0.09 \left(\log \frac{L_{500}}{L_{\odot}} - 9 \right) + 10.09 \pm 0.08 \\ \log \frac{M_{\text{HI}}}{M_{\odot}} &= 0.69 \pm 0.13 \left(\log \frac{M_{\text{dust}}}{M_{\odot}} - 9 \right) + 10.50 \pm 0.07 \\ \log \frac{M_{\text{HI}}}{M_{\odot}} &= \log \xi_{\text{HI}}^{\text{d}} + \log \left(\frac{M_{\text{dust}}}{M_{\odot}} \right)\end{aligned}$$

Here and in all subsequent equations we use mass and luminosity in solar units and use years as the denominator in all SFRs.

3.2 M_{H_2} estimates from dust

Among the M/L estimates of M_{H_2} the $160\mu\text{m}$ luminosity is best, because although its R value is not significantly different from that of L_{100} or L_{250} , its σ is the smallest. The longer wavelength luminosities become increasingly poor estimates of M_{H_2} . This connection between molecular gas and shorter wavelengths is consistent with the use of L_{IR} as an SFR indicator (e.g., Reddy et al. 2010). Using M_{dust} instead (with or without ξ) gives an even poorer predictor of M_{H_2} .

For comparison, the relationship between M_{H_2} and L_{160} from Groves et al. (2015) is also shown in Figure 2 as a wide green line, and agrees with our data points. Note that their best-fit relation has a steeper slope than ours, as their sample includes a number of dwarf galaxies ($M_* < 10^9 M_{\odot}$) with small molecular gas masses ($M_{\text{H}_2} \sim 10^7 M_{\odot}$) which drive this steeper slope. If these dwarf galaxies were removed to match the stellar mass range of our sample, the Groves et al. (2015) best-fitting relationship would be consistent with ours. Our best fitting relation with L_{160} is given below, along with the L_{500} prediction (as it is more commonly used).

$$\begin{aligned}\log \frac{M_{\text{H}_2}}{M_{\odot}} &= 0.92 \pm 0.04 \left(\log \frac{L_{160}}{L_{\odot}} - 9 \right) + 8.41 \pm 0.04 \\ \log \frac{M_{\text{H}_2}}{M_{\odot}} &= 0.99 \pm 0.05 \left(\log \frac{L_{500}}{L_{\odot}} - 9 \right) + 9.92 \pm 0.06\end{aligned}$$

3.3 Total M_{gas} estimates from dust

The estimates of M_{gas} show a similar behavior to those of M_{HI} , as HI is the dominant gas component in our galaxies. The best M_{gas} predictor is L_{500} ; although its R value is not significantly better than the ξ -based estimates, it does have smaller scatter in the relationship. This is consistent with its connection to diffuse ISM emission. The M_{dust} estimates of M_{gas} are only slightly worse, perhaps due to the additional uncertainties from fitting SEDs to determine dust masses. Regardless of the choice between L_{500} and M_{dust} , these correlations with M_{gas} are the strongest and tightest of any combination of gas phase and indicator discussed thus far. Our three best-fitting M_{gas} relations are given below, where $\xi_{\text{tot}}^{\text{d}}$ was determined in Section 2.

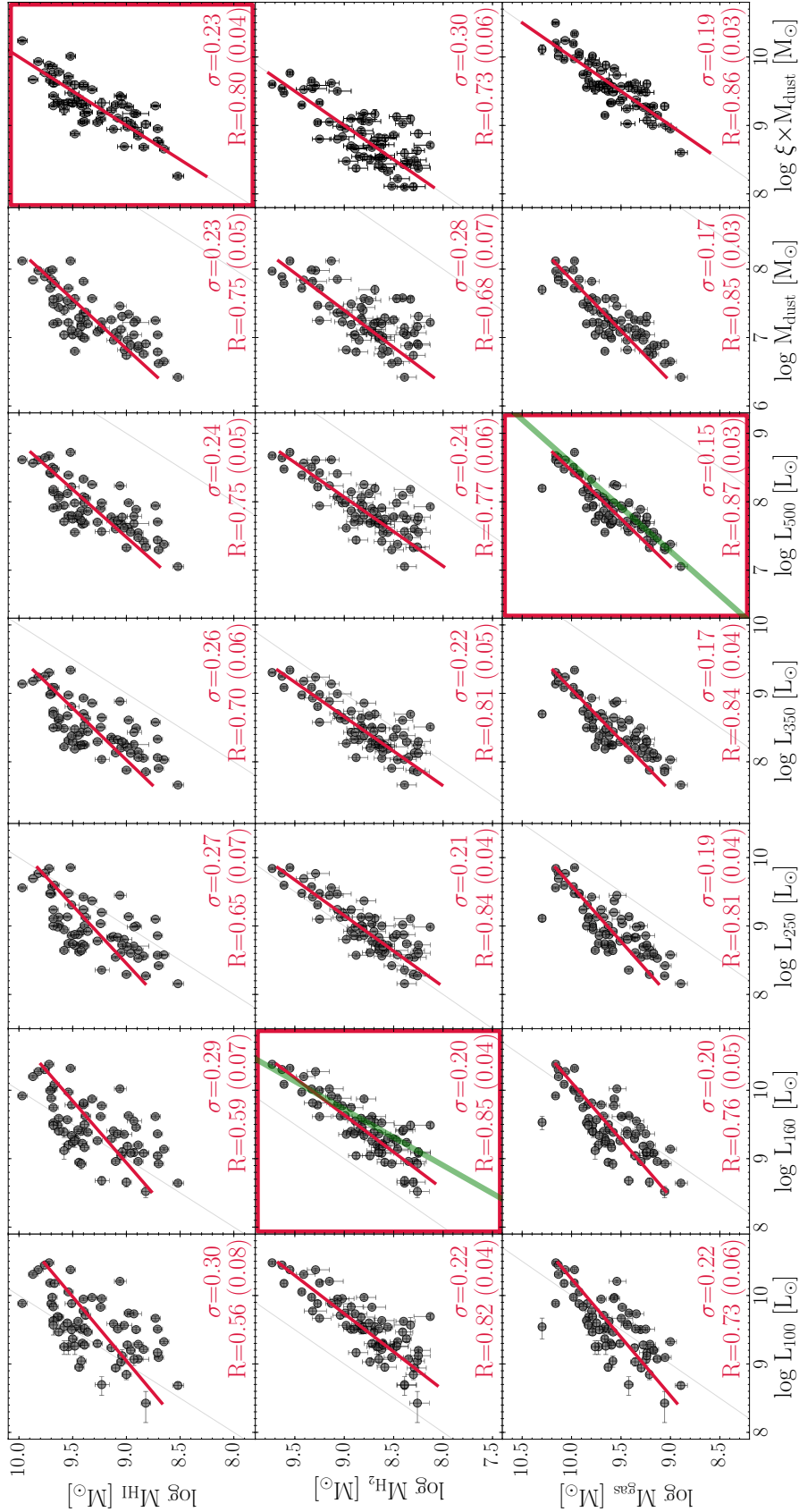


Figure 2. Correlations between gas phase masses (HI in top row, H₂ in middle row, total M_{gas} in bottom row) and monochromatic IR luminosities (from 100 μ m to 500 μ m) and dust masses (with and without metallicity-dependent ξ for that phase). Light grey lines show 1:1 lines in each plot, and the axes have the same tick sizes in all panels. In the last column ($\xi \times M_{\text{dust}}$) the red line is a unity line and no fitting is performed as ξ was already fit in Figure 1 for each phase. The strongest and tightest relationships are indicated by bold boxes. Wide green lines show the agreement with relations from Groves et al. (2015).

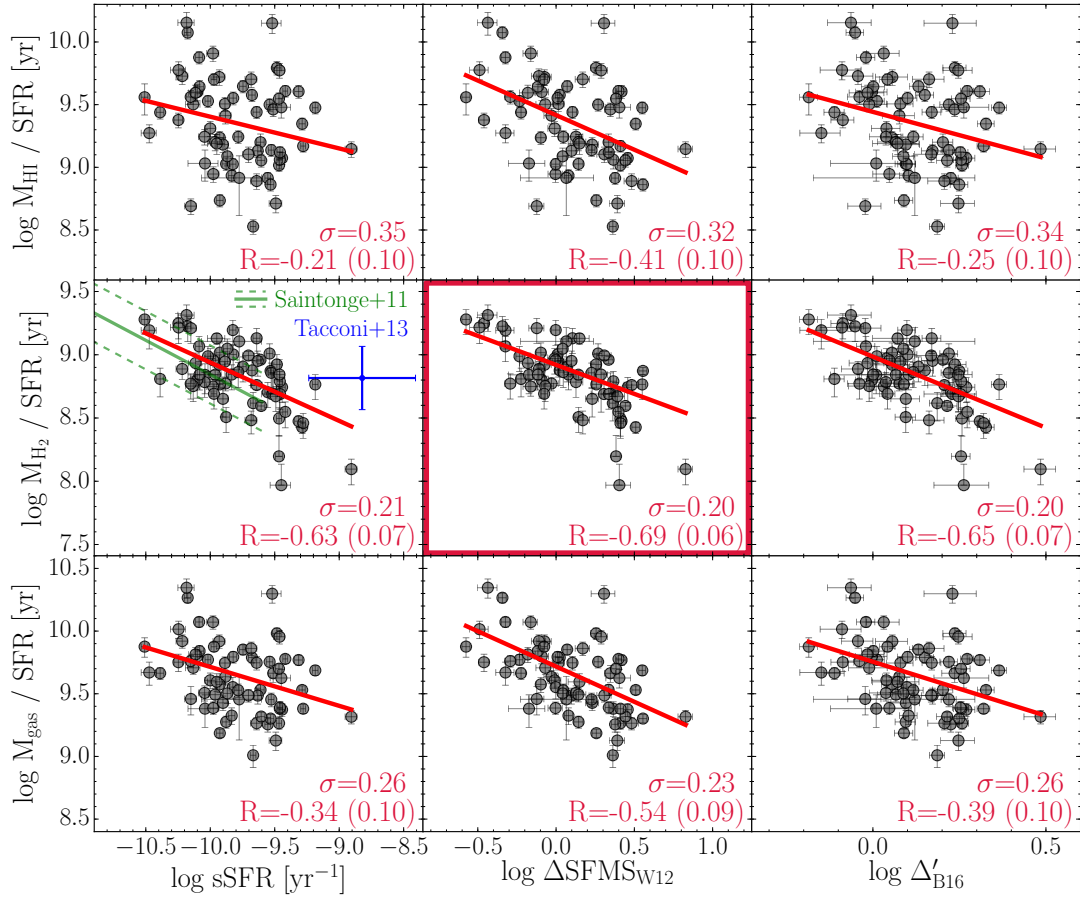


Figure 3. Gas mass divided by SFR (i.e., depletion time) using various gas phases is plotted against SFR-related quantities. Left column x-axis shows specific SFR (sSFR), and our $M_{\text{H}_2}/\text{SFR}$ values agree with the average value from [Tacconi et al. \(2013\)](#) and the trend from [Saintonge et al. \(2011a\)](#). Center column shows ΔSFMS using the [Whitaker et al. \(2012\)](#) SFMS. Right column shows Δ'_{B16} from [Berta et al. \(2016\)](#), a weighted combination of sSFR and M_* .

$$\begin{aligned} \log \frac{M_{\text{gas}}}{M_{\odot}} &= 0.71 \pm 0.05 \left(\log \frac{L_{500}}{L_{\odot}} - 9 \right) + 10.39 \pm 0.05 \\ \log \frac{M_{\text{gas}}}{M_{\odot}} &= 0.67 \pm 0.08 \left(\log \frac{M_{\text{dust}}}{M_{\odot}} - 9 \right) + 10.78 \pm 0.05 \\ \log \frac{M_{\text{gas}}}{M_{\odot}} &= \log \xi_{\text{tot}}^{\text{d}} + \log \left(\frac{M_{\text{dust}}}{M_{\odot}} \right) \end{aligned}$$

[Groves et al. \(2015\)](#) found a similar relationship between L_{500} and M_{gas} as ours, as shown by the wide green line in [Figure 2](#). Their relationship agrees with our data points after it is corrected to include helium to match our convention.

Going forward, we prefer the L_{500} estimates of M_{gas} , as it gives the best correlation and also does not require any additional assumptions to determine dust mass. For M_{H_2} estimates, we prefer L_{160} if available, but L_{500} is acceptable. However, there are significant residual trends in these predictions, as discussed in [Section 6](#).

4 DEPLETION TIME ESTIMATES

As a second method to estimate gas mass without direct observations, we can use the inverted integrated Kennicutt-Schmidt law (i.e., gas depletion time, t_{dep}). We start by using each galaxy’s SFR as a predictor of its amount of (star-forming) gas. In order to do this, we must determine the

distance between each galaxy and the so-called star-forming main sequence (SFMS; [Salim et al. 2007](#); [Noeske et al. 2007](#)). The SFMS is typically defined as the ridge-line in the SFR- M_* diagram and is populated by “star-forming” galaxies. We use two different definitions of SFMS. In general, the SFMS can be parameterized as follows.

$$\log \frac{\text{SFR}_{\text{MS}}}{M_{\odot} \text{yr}} = \alpha \left(\frac{M_*}{M_{\odot}} - 10.5 \right) + \beta$$

Using UV+IR SFRs for $\sim 22,000$ galaxies at $0 < z < 2.5$, [Whitaker et al. \(2012\)](#) derived a redshift-dependent SFMS with parameters given below.

$$\alpha_{\text{W12}z} = 0.70 - 0.13z, \quad \beta_{\text{W12}z} = 0.38 + 1.14z - 0.19z^2$$

We also considered the SFMS from [Catinella et al. \(submitted, see also Janowiecki et al. in prep.\)](#), which is based on UV+IR SFRs of a low redshift sample of ~ 1200 stellar-mass selected galaxies from xGASS ([Janowiecki et al. 2017](#)), with best-fit parameters given below.

$$\alpha_{\text{J17}} = 0.656, \quad \beta_{\text{J17}} = 0.162$$

While this is based on a representative sample of local ($z \sim 0$) galaxies, the [Whitaker et al. \(2012\)](#) SFMS includes a redshift dependence, making it more useful in extending our predictive relationships for ISM masses to galaxies at higher

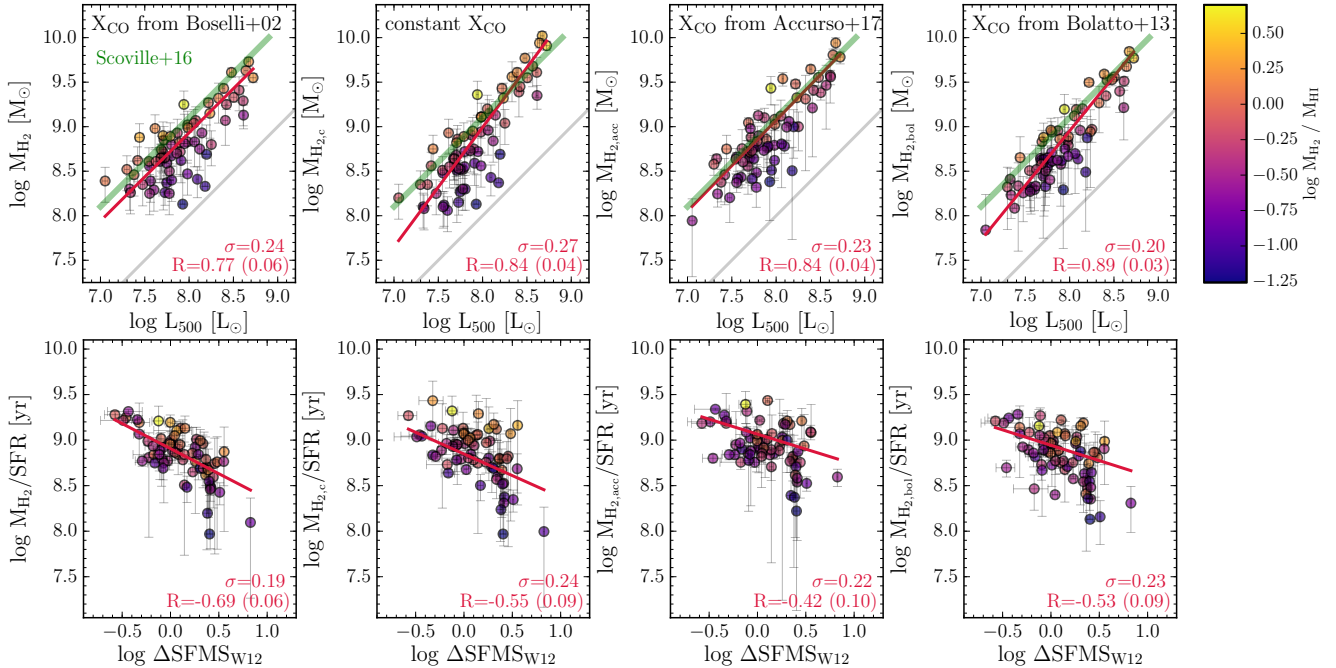


Figure 4. Top row: correlations between L_{500} and M_{H_2} , using different X_{CO} conversion factors. Wide green line indicates the relationship from [Scoville et al. \(2016\)](#), which uses a constant X_{CO} . Bottom row: Correlations between depletion time (M_{H_2}/SFR) and $\Delta SFMS$, using the same prescriptions. In all panels, points are colored by their M_{H_2}/M_{HI} ratio, using the M_{H_2} prescription from that panel.

redshifts. We use only the [Whitaker et al. \(2012\)](#) SFMS going forward, as both give similar results for our sample.

Using this definition of SFMS, we compute $\Delta SFMS$, which quantifies each galaxy’s distance above or below the SFMS at its M_* and redshift.

$$\log \Delta SFMS = \log \frac{SFR}{M_{\odot}/yr} - \log \frac{SFR_{MS}(M_*, z)}{M_{\odot}/yr}$$

In a similar vein, [Berta et al. \(2016\)](#) derive an expression for depletion times based primarily on $\Delta SFMS$, but also including a dependence on M_* and redshift (their Equation 3). We show this quantity as Δ'_{B16} .

Figure 3 shows our observed depletion times (M_{gas}/SFR) using different gas masses (H_I , H_2 , total). These are plotted against sSFR (left column), $\Delta SFMS$ (center column), and Δ'_{B16} (right column). As with Figure 2, best-fit lines and quality estimates are shown on each panel. Note that for each predictive indicator shown on the x-axis, the relation with M_{H_2} has the tightest scatter and strongest correlation. Unsurprisingly, the SFR-based indicators are less closely related to M_{HI} . Since our galaxies are H_I -dominated, the predictions for M_{gas} are similarly weak. Again we caution against blindly applying our calibrations to populations of galaxies which are significantly different from those in our sample. We next focus on two of these predictions of M_{H_2} .

4.1 M_{H_2} estimates from t_{dep} (sSFR)

The relations shown in Figure 3 are consistent with previous results, as seen in the panel showing M_{H_2}/SFR vs sSFR. Here the constant depletion time estimate from [Tacconi et al. \(2013\)](#) is shown (at the average sSFR of their sample), as well as the relation from [Saintonge et al. \(2011a\)](#), both of

which are consistent with our observations. Our best-fitting relationship between M_{H_2}/SFR (in units of years) and sSFR (in inverse years) is given below.

$$\log \frac{M_{H_2}}{SFR} = -0.46 \pm 0.74 \times \log \text{sSFR} + 4.32 \pm 0.08$$

4.2 M_{H_2} estimates from t_{dep} ($\Delta SFMS$)

The strongest and tightest correlation is found between M_{H_2}/SFR and $\Delta SFMS$, as the H_2 is directly involved in current star formation. The best-fitting relationship between $\Delta SFMS_{W12}$ and M_{H_2}/SFR (in years) is given below.

$$\log \frac{M_{H_2}}{SFR} = -0.46 \pm 0.03 \times \log \Delta SFMS_{W12} + 8.92 \pm 0.08$$

This relationship has similar scatter and strength as the L_{500} – M_{gas} and M_{dust} – M_{gas} relationships determined in Section 3, but also is affected by the residual trends discussed in the following section.

4.3 Alternative M_{H_2} prescriptions

We briefly consider the effects of alternative X_{CO} conversion factors to determine M_{H_2} from CO observations, as introduced in Section 2.1. In addition to the luminosity-dependent X_{CO} we primarily use, we show here the results of using a constant conversion factor ($M_{H_2,c}$), the metallicity-dependent conversion ($M_{H_2,acc}$) from [Accurso et al. \(2017\)](#), and the conversion from [Bolatto et al. \(2013\)](#) ($M_{H_2,bol}$) which depends on metallicity and stellar surface density (determined from optical effective radius). Figure 4 shows the predictive relations for these determinations of M_{H_2} using L_{500} (top row) and depletion time from $\Delta SFMS$

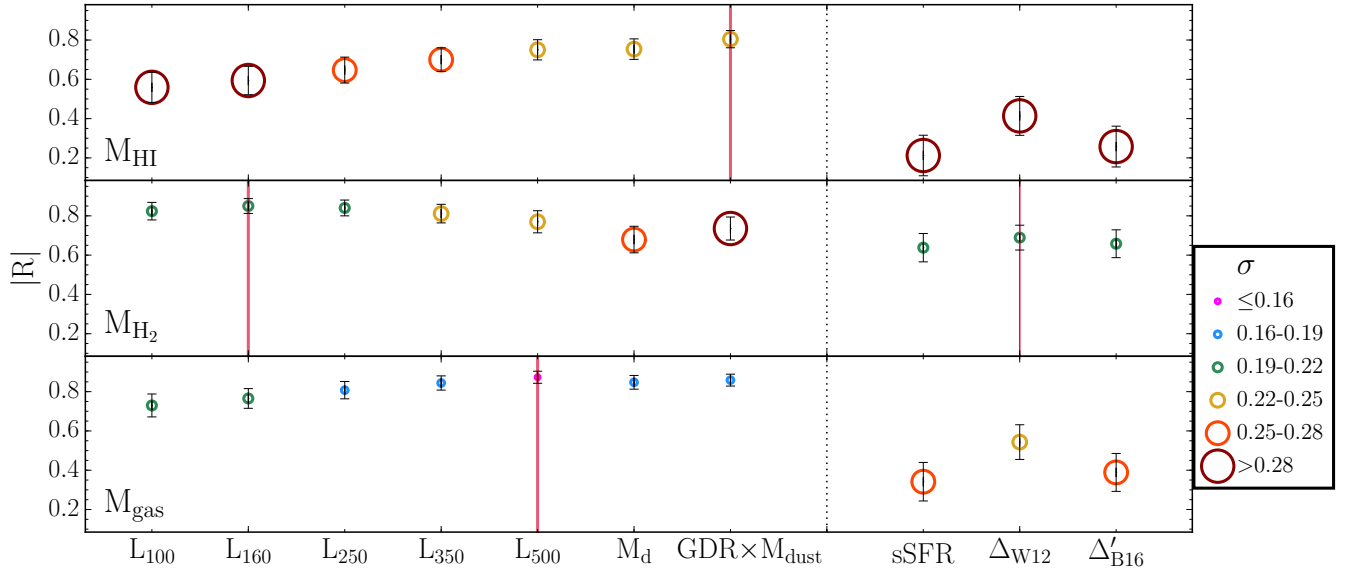


Figure 5. The absolute value of Pearson’s R value is shown for each indicator, from the correlations shown in Figures 2 and 3. The size and color of each point corresponds to its scatter (σ , in dex), as indicated in the legend. The best relationships are marked with solid red vertical lines. Uncertainties on $|R|$ are shown as error bars and show the standard deviations from 10,000 random samplings.

(bottom row). In all cases, the M_{H_2} values do not include the contribution from helium.

Using different conversion factors does not dramatically alter these predictive relationships. Adopting the metallicity-dependent conversion from [Accurso et al. \(2017\)](#) moderately improves the strength (and scatter) of the L_{500} prediction, but it significantly worsens the strength of the relationship with depletion time. Similarly, the [Bolatto et al. \(2013\)](#) prescription marginally improves the strength and scatter of the L_{500} relation and worsens the trend with $\Delta SFMS$.

Also shown in the top row of Figure 4 is the L_{500} -based M_{H_2} prediction from [Scoville et al. \(2016\)](#), which is determined from observations of 70 galaxies between $z = 0 - 2$. That calibration adopts the constant Galactic value of X_{CO} , so it is most appropriate to compare it with the left middle panel. As expected, the [Scoville et al. \(2016\)](#) relationship works better for galaxies with $M_{H_2} \gtrsim M_{HI}$; HI-dominated galaxies can fall as much as an order of magnitude below the prediction. This illustrates the difficulty in using FIR dust luminosity to predict M_{H_2} alone – without knowledge of the atomic-to-molecular ratio, it is difficult to estimate the mass in each phase from a dust luminosity.

5 CLOSING THE LOOP

Figure 5 visually summarizes the quality of the predictive relationships calibrated thus far. Above each indicator on the x-axis (i.e., monochromatic luminosity, dust mass, sSFR, or depletion time estimate) the strength and scatter of its correlation with each gas mass are shown (for HI, H_2 , and total gas). The y-axis position shows the absolute value of Pearson’s R value, and the size of each point corresponds to the standard deviation of our observations about the best-fit (or unity) line (σ). Larger symbols show relationships with higher scatter.

As is shown in Figure 5 (and in Sections 3 & 4), M_{HI}

is better predicted by longer wavelength IR emission (reaching the best prediction at $500\mu m$), and slightly better still by dust mass and metallicity. As atomic gas is less directly connected to ongoing star formation, predictions based on depletion time are poorer for M_{HI} . Molecular gas mass is best predicted either by L_{160} or depletion time estimates, both of which have similar scatter but the M/L method gives a stronger correlation, partly due to its larger dynamic range. Total gas is best predicted by L_{500} , and depletion time estimates perform poorly, as the galaxies in our sample are HI-dominated.

We next compare the two methods and evaluate whether these separate predictions are mutually consistent. Figure 6 shows two different predictions of M_{H_2} (left panel, from $\Delta SFMS$ and L_{500}) and two different predictions of M_{gas} (right panel, from M_{dust} and L_{500}). Since all of these estimates have been calibrated using the same sample of galaxies, their good consistency is not surprising.

The two estimates of M_{H_2} are observationally independent, as the t_{dep} prediction depends only on SFR and M_* , which are separate from the observations of L_{500} . It is possible to calibrate those two predictive relationships so that mutually consistent estimates of M_{H_2} are obtained, whether using SFR or FIR luminosity. Note that using a fixed depletion time (e.g., [Tacconi et al. 2013](#)) gives a relationship which is $\sim 15\%$ steeper than the 1:1 line, and which over-estimates $M_{H_2}(t_{dep})$ at higher H_2 masses.

The two estimates of total M_{gas} are less independent, as the L_{500} emission is closely related to the dust content. As such, the two indicators correlate with each other ($\sigma=0.07$ dex) more tightly than with M_{gas} ($\sigma=0.15-0.17$ dex). This is reassuring as it means the choice of indicator is not crucial, and both L_{500} and M_{dust} are good estimators of M_{gas} . Note also that adopting a metallicity-dependent ξ_{tot}^d (as derived in Section 2) introduces a $\sim 25\%$ steeper slope to the relation between $M_{gas}(M_{dust})$ and $M_{gas}(L_{500})$. This systematic difference implies that ξ_{tot}^d

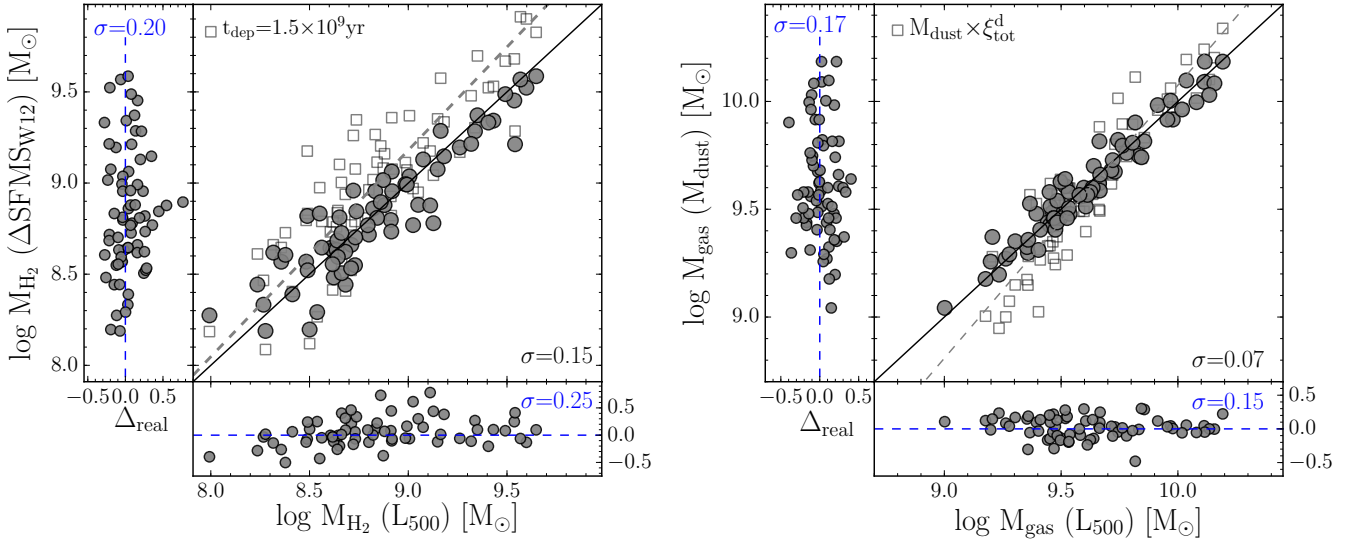


Figure 6. M_{H_2} (left) and M_{gas} (right) comparisons from our calibrations. In both main panels, our predictions for the gas phase masses are shown, using different indicators on both axes (σ shows the scatter about the unity line, in dex). The residual panels show the differences between the predicted and measured gas phase masses (Δ_{real}). Also shown (in light grey boxes, and best-fitting dashed lines) are the results when using alternative calibrations for the y-axis quantities. In the left panel, small boxes show the effect of assuming a constant depletion time. In the right panel, small boxes show the results of using $\xi_{\text{tot}}^{\text{d}}$ which depends on metallicity (and assuming $M_{\text{gas}} = M_{\text{dust}} \times \xi$). Note that the two estimates of M_{gas} (from M_{dust} and from L_{500}) are better correlated with each other ($\sigma=0.07$) than they are with M_{gas} , as L_{500} also tracks the dust content.

scales with galaxy stellar mass (via the mass-metallicity relation), as has been shown by Cortese et al. (2016) and Rémy-Ruyer et al. (2013). In order to eliminate the slope difference between these two estimates, the metallicity-dependent $\xi_{\text{tot}}^{\text{d}}$ relationship would need a 3 times steeper slope, which dramatically increases the scatter of the points around the unity line in Figure 6.

These comparisons demonstrate that the choice of calibration method can have significant effects on the indirect predictions of cold gas masses. Even within the same sample of galaxies there can be systematic deviations when using different assumptions, such as a constant depletion time or a metallicity-dependent ξ . Nonetheless, with appropriate choices, independent predictive methods can be calibrated to produce estimates which are in agreement with each other.

6 RESIDUAL TRENDS IN CALIBRATIONS

These predictive relationships perform as expected in our sample of local, star-forming, HI-dominated galaxies. However, we are most interested in applying these relationships to galaxies at higher redshifts, where the partition between atomic and molecular gas is unknown and other physical properties may differ (e.g., M_* , sSFR). Across our sample, the ratio of $M_{\text{H}_2}/M_{\text{HI}}$ varies between $\sim 3\%$ and $\sim 300\%$, which is similar to the range of values observed in galaxies from the xGASS sample (Catinella et al. submitted). Galaxies in xGASS also show a weakly increasing median value of the molecular-to-atomic ratio as a function of stellar mass, from $\sim 10\%$ at $10^9 M_{\odot}$ to $\sim 30\%$ at $10^{11.5} M_{\odot}$.

6.1 Quantifying residual systematics

Quantifying the strength of any residual secondary dependences requires careful parametrization to avoid being affected by underlying dependences between M_{gas} and its constituent phases. For example, plotting the accuracy of the L_{500} prediction of M_{HI} as a function of the $M_{\text{H}_2}/M_{\text{HI}}$ ratio has a strong intrinsic correlation (from the inclusion of M_{HI} on both axes) which makes it difficult to directly interpret the residuals in a physical sense. We explore these intricacies in a Monte Carlo analysis described in Appendix A, and demonstrate that our approach successfully quantifies physical residual dependences without suffering from these effects.

6.2 Residuals between phases

We quantify the underlying dependence between predictions in each phase by plotting the accuracy of the predictive relationships for M_{HI} and M_{H_2} as functions of M_{H_2} and M_{HI} , respectively. In this way we are comparing observationally independent quantities, and the residual trends can be meaningfully interpreted (see Appendix A for more discussion of this method). The top two panels in the left column of Figure 7 show the differences between the L_{500} -based prediction and the real gas masses for HI and H₂. The M_{HI} differences are plotted against M_{H_2} , and the M_{H_2} differences against M_{HI} (i.e., independently observed quantities). Each residual trend is fitted and their slopes (m), scatters (σ), and correlations (R) are shown, with uncertainties. These fits use least squares minimization of the ordinate and are weighted by the uncertainties of the observed gas phase masses only (i.e., they do not include the uncertainties on the predicted gas masses).

For galaxies with larger M_{H_2} , L_{500} under-predicts M_{HI} ,

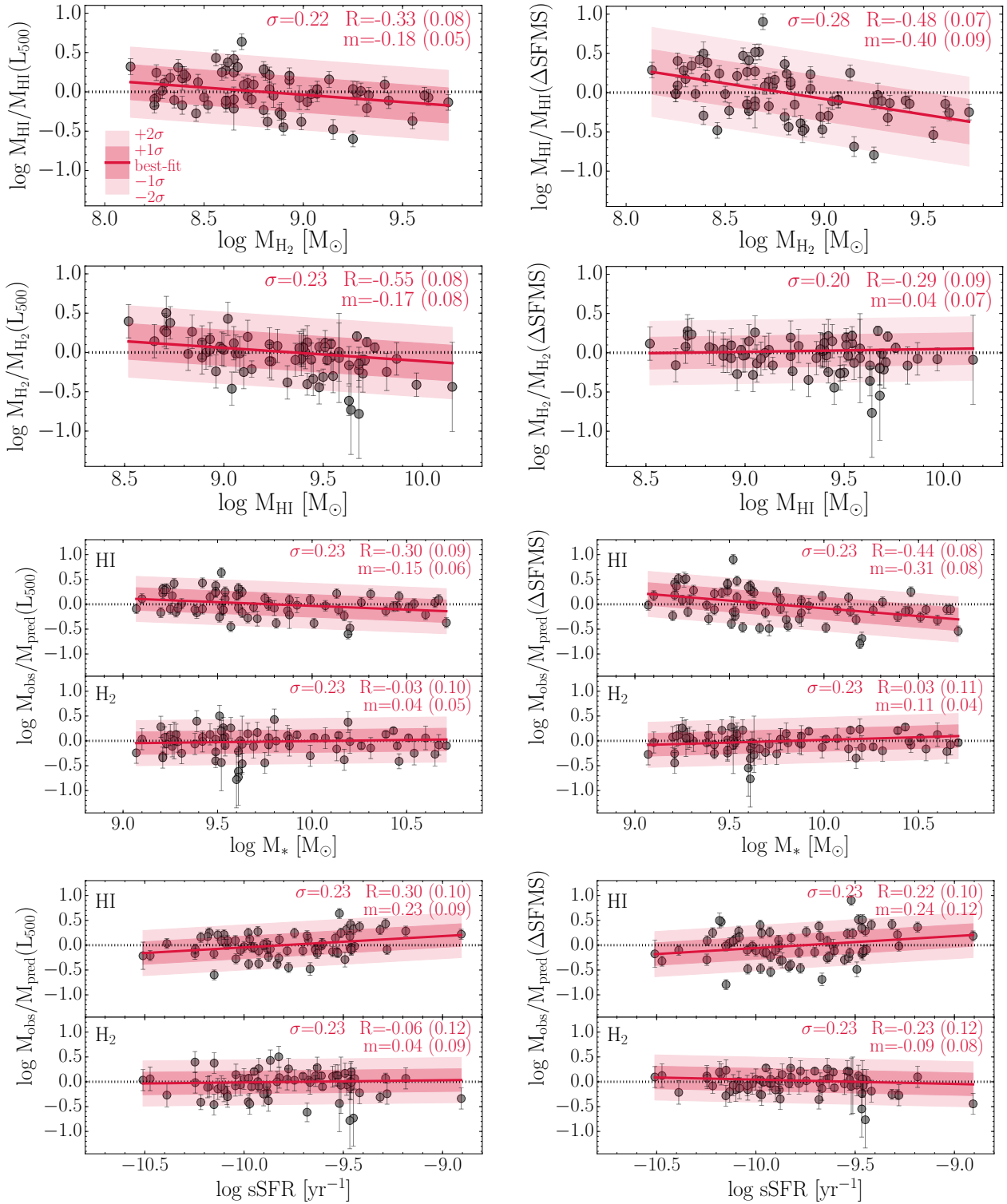


Figure 7. Left panels: Residuals of L_{500} (dust) predictions for M_{HI} and M_{H_2} as a function of the mass of the other phase. Top panel shows M_{HI} divided by its prediction from L_{500} , demonstrating an anti-correlation with M_{H_2} . Bottom panel shows M_{H_2} divided by its prediction from L_{500} , with similarly strong anti-correlation with M_{HI} . Right panels: Residuals of the $\Delta SFMS$ (depletion time) predictions for M_{HI} and M_{H_2} as a function of the mass of the other phase. A stronger residual trend is found when predicting M_{HI} from depletion time, while no trend exists in the M_{H_2} prediction.

and for galaxies with larger M_{HI} , L_{500} under-predicts M_{H_2} . This behavior illustrates that L_{500} is most tightly correlated with the total gas mass (e.g., see Section 3.3); any M_{HI} or M_{H_2} prediction based on L_{500} will have a systematic uncertainty depending on the partition of atomic and molecular gas. These systematic trends are of modest amplitude (slopes of 17-18% per dex, with $\geq 2\sigma$ significance) and large scatter (0.2 dex), but are evident even within our small sample of local star-forming galaxies. At higher redshift and for larger more star-forming systems, extrapolations of these discrepancies could be larger.

In a similar way, the top two panels in the right column of Figure 7 compare the depletion time-based predictions of gas masses (using ΔSFMS) for M_{HI} and M_{H_2} with their true values as a function of M_{H_2} and M_{HI} , respectively. The discrepancies in M_{HI} predictions show steep systematic variations (slope of 40% per dex with $\geq 4\sigma$ significance), which is not unexpected since depletion time is less physically connected to the neutral atomic gas content. Conversely, the errors in the M_{H_2} prediction do not depend on M_{HI} , as this method is best suited to predict M_{H_2} , the gas which is directly involved in star formation. When using SFR to predict gas mass, there is an implicit assumption about the rate of H_2 conversion into stars as well as the conversion between HI and H_2 . This introduces an underlying dependence on the partition between M_{HI} and M_{H_2} , as was seen in the M/L estimates.

These residual trends serve as a reminder that ISM mass predictions from dust luminosities and star formation rates are not equivalent and are sensitive to different gas phases. In the worst cases, using L_{500} to predict M_{H_2} is dependent on M_{HI} ($R = -0.55$) with a modest slope ($m = 0.17$), giving systematic over/under-predictions of ~ 0.15 dex at the extremes of our sample. Similarly, using t_{dep} to predict M_{HI} results in an even steeper slope ($m = -0.40$) and similar correlation ($R = -0.48$), over/under-predicting by up to ~ 0.3 dex. Without prior knowledge of the partition between molecular and atomic gas it is difficult to apply these predictions. Other studies have shown that the $M_{\text{H}_2}/M_{\text{HI}}$ ratio in galaxies can depend on the metallicity and turbulence of their ISM, which affect the conversion between atomic and molecular gas (Krumholz et al. 2009; Bialy et al. 2017).

6.3 Residuals with other physical properties

We also explored similar residual dependences using other galaxy properties. In particular, we considered galaxy stellar mass and sSFR. The lower four panels of Figure 7 show, as a function of these physical properties, the ratios between the observations of M_{HI} and M_{H_2} and their L_{500} and ΔSFMS -based predictions. As with the top panels, we fit these residual trends to quantify their strengths.

For both L_{500} and ΔSFMS , we see negative (positive) residuals for the M_{HI} (M_{H_2}) predictions with increasing stellar mass. While sometimes weak, these trends are expected, given the moderately increasing $M_{\text{H}_2}/M_{\text{HI}}$ ratio observed as a function of stellar mass (Catinella et al. submitted).

All of the residual trends with M_* are weaker (smaller R values and almost always flatter slopes) than those with M_{HI} or M_{H_2} , indicating that a stellar mass dependence is not enough to account for the residuals observed between the phases. The sSFR residuals in the predictions of M_{HI}

suggest that elevated star formation results in L_{500} and ΔSFMS under-predicting M_{HI} , while in more passive galaxies, it may be over-predicted (by ~ 0.2 dex, even within our sample's relatively small range of sSFR).

These modest systematic trends with M_* and sSFR suggest that using L_{500} or ΔSFMS as ISM mass estimators will be affected by underlying dependences on other galaxy properties. Our calibrations are naturally best-suited to predicting cold gas masses for galaxies which are similar to those included in our sample. Any extrapolation or extension of these relationships to significantly different populations of galaxies (e.g., with higher or lower M_* or sSFR) may suffer from systematic biases. Nonetheless, these predictions are robust and can reliably generate indirect estimates of cold gas masses.

7 SCIENTIFIC IMPLICATIONS

7.1 Applications to high- z galaxy observations

Figure 8 shows the basic relations between gas masses and L_{500} for our sample and galaxies at other redshifts where all three observations (21cm, CO, and $500\mu\text{m}$) are available. In addition to the sample used in this work, we show 26 galaxies from the xGASS sample ($z=0.01-0.05$, Catinella et al. submitted) which have L_{500} observations from the NASA/IPAC Infrared Science Archive,¹ survey data from *Herschel*-ATLAS (Valiante et al. 2016; Bourne et al. 2016) and the *Herschel* Stripe 82 Survey (Viero et al. 2014, HERS).

We also include two galaxies with observations at higher redshifts ($z>0.1$). First, AGC 191728 comes from the HIGHz sample of Catinella & Cortese (2015) at $z=0.176$. Its HI observations come from Arecibo and its CO(1-2) observations from the Atacama Large Millimeter Array (Cortese et al. 2017). This galaxy was serendipitously imaged as part of the *Herschel*-ATLAS observations and released in H-ATLAS DR1 (Valiante et al. 2016).

Second, COSMOS J100054.83+023126.2 comes from the Cosmic Evolution Survey (COSMOS Scoville et al. 2007) and is at $z=0.376$ (this is the highest redshift detection of HI emission from a galaxy to date). It has recently been observed in 21cm with the Jansky Very Large Array as part of the COSMOS HI Large Extragalactic Survey (CHILES) and in CO with the Large Millimeter Telescope (Fernández et al. 2016). In another serendipitous observation, DR2 of the *Herschel* Multi-tiered Extragalactic Survey (HERMES, Oliver et al. 2012) includes $500\mu\text{m}$ observations of this galaxy, with fluxes available through their SUSSEXtractor catalog.

Note that the observed $500\mu\text{m}$ emission from these two sources corresponds to rest-frame observations at $425\mu\text{m}$ and $363\mu\text{m}$, respectively. While we use these fluxes in our L_{500} -based relationships, adopting the L_{350} -based predictions would make only a small difference. Within our sample, the ratio of L_{350}/L_{500} is 1.073 ± 0.006 .

These two higher redshift galaxies provide an illustrative example of the application of the L_{500} -based predictions of cold gas masses. These two galaxies are quite different: while they have very similar M_{HI} (and stellar mass estimates from optical photometry), the CHILES galaxy has ~ 4 times

¹ <http://irsa.ipac.caltech.edu/>

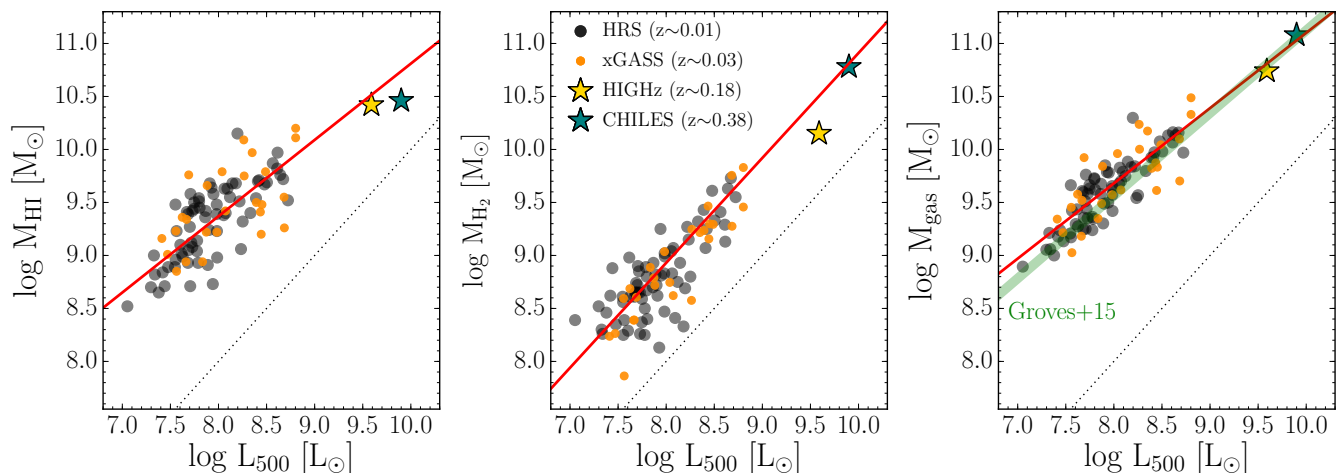


Figure 8. All three panels show galaxies in our sample (in grey) and other colors show other galaxies including some at higher redshifts. The dotted line shows the 1:1 relationship. Our best-fitting relationships for M_{HI} (left), M_{H_2} (center), and M_{gas} (right) are shown as red lines. Higher redshift galaxies appear to follow similar behavior as our local sample, with a tight L_{500} - M_{gas} relation and correlated scatter in the M_{HI} and M_{H_2} relations.

larger M_{H_2} than the HIGHz galaxy. Their $M_{\text{H}_2}/M_{\text{HI}}$ ratios are 50% and 200%, respectively. Remarkably, the L_{500} prediction for M_{gas} is very accurate for both! However, L_{500} -based estimates of M_{HI} and M_{H_2} can be wrong by ~ 0.4 dex. The HI-dominated HIGHz galaxy lies along the L_{500} - M_{HI} relationship, but falls ~ 0.4 dex below L_{500} - M_{H_2} . Conversely, the H_2 -dominated CHILES galaxy is consistent with the L_{500} - M_{H_2} relation but falls ~ 0.3 dex below L_{500} - M_{HI} . *Without additional knowledge of the molecular-to-atomic ratio of these galaxies, L_{500} cannot reliably predict their M_{HI} or M_{H_2} separately.*

Extending this argument further, observations have suggested that higher-redshift galaxies have higher $M_{\text{H}_2}/M_{\text{HI}}$ ratios compared with the HI-dominated galaxies observed at low-redshift, but within $z < 0.2$ this ratio seems to span the same range of values (Cortese et al. 2017; Cybulski et al. 2016). When using these types of relations to predict molecular gas masses at high redshift, corrections may be necessary to account for different mass contributions from ISM phases. When predicting gas masses in high redshift galaxies, appropriately calibrated relations must be used. While it is possible to separate the atomic and molecular gas phases in our local sample, the distinction becomes difficult at higher redshift. There is inherent uncertainty in extending a low-redshift prediction to higher redshift galaxies, which may have different atomic-to-molecular ratios or other physical differences from local galaxies.

7.2 Consequences of incorrect phase assumptions

In Figure 9 we quantify the possible errors introduced by applying L_{500} -based gas mass predictions to galaxies without knowledge of their molecular-to-atomic partitions. In each panel we either apply the assumption that galaxies are HI-dominated and use the relationship calibrated for M_{HI} (orange circles) or are H_2 -dominated and use the M_{H_2} relationship (purple squares). For completeness we also show the comparison between total gas mass predictions and the observed $M_{\text{HI}}+M_{\text{H}_2}$ (green triangles). Each of these com-

parisons has a systematic offset from unity: the M_{H_2} and M_{HI} predictions scatter around the average molecular and atomic gas fractions for this sample, and the M_{gas} predictions include the $\sim 30\%$ correction for the contribution of helium.

When adopting the HI-dominated assumption (orange circles), the y-axis shows the difference between the true $M_{\text{HI}}+M_{\text{H}_2}$ and the L_{500} -predicted M_{HI} , as M_{H_2} is assumed to be negligible. This assumption is most accurate for galaxies with $M_{\text{gas}} \sim 10^9 M_{\odot}$, with large stellar mass, or with passive sSFR, where the L_{500} - M_{HI} relationship accurately predicts the total gas mass. Estimates generated from this assumption become significantly worse for more star-forming galaxies or those with larger gas masses (i.e., similar to those observed at higher redshifts) where the predictions can be up to ~ 0.5 dex too small. For galaxies with more extreme $M_{\text{H}_2}/M_{\text{HI}}$ ratios, the effects of this incorrect assumption could be even larger.

While the H_2 -dominated assumption (purple squares) is clearly not valid for any of the galaxies in our sample (note that none reach unity in the ratio being plotted), this assumption interestingly shows strong systematic variations with M_{\star} and sSFR. These systematic trends are stronger and more significant than those found in Figure 7, and are a manifestation of the incorrect assumption about the dominant phase. Even the L_{500} - M_{gas} relationship (green triangles) shows a dependence on sSFR at the $\sim 2.5\sigma$ level, demonstrating the ubiquity of underlying systematic residuals.

While it is not unsurprising that incorrect assumptions about the dominant gas phase yield incorrect results, these trends demonstrate quantitatively the nature of errors arising from these assumptions. Most importantly, in addition to the expected systematic offset, Figure 9 shows that residual trends are present which depend on other galaxy properties. *Every application of these indirect gas mass predictions relies on implicit assumptions to produce M_{HI} or M_{H_2} estimates.*

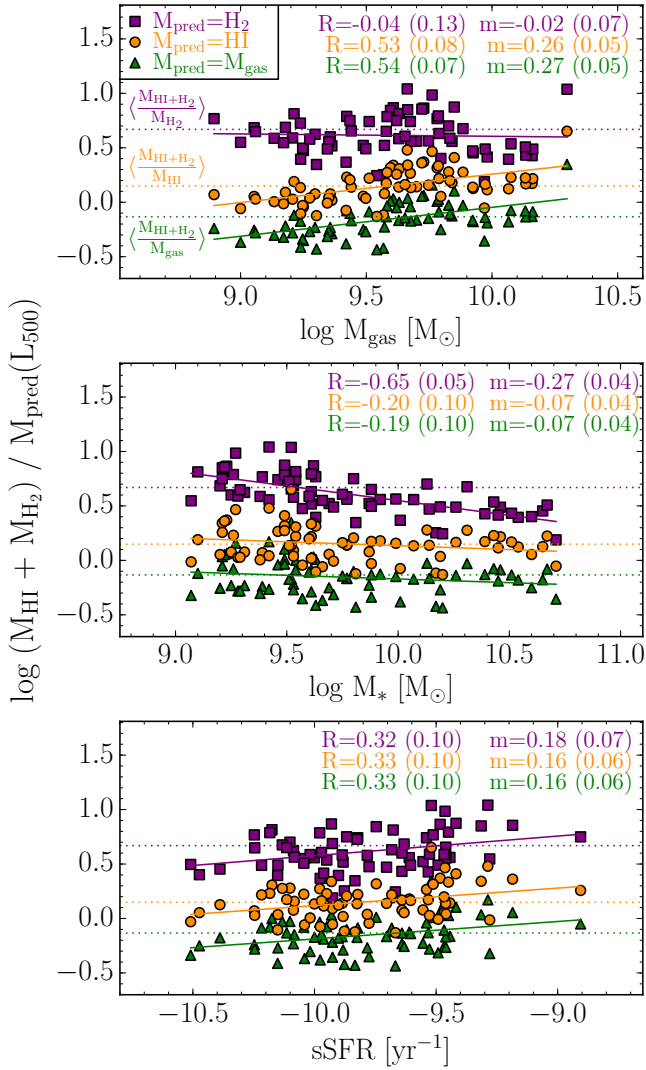


Figure 9. Each panel plots the ratio between the observed $M_{\text{HI}} + M_{\text{H}_2}$ and the L_{500} -based predictions of M_{HI} (M_{H_2}) as orange circles (purple squares), as functions of total gas mass, stellar mass, and sSFR. Relations with M_{gas} are shown as green triangles. Least squares fits are shown along with best-fit slopes and uncertainties.

7.3 The K-S with different calibrations

Figure 10 shows the integrated K-S star formation law (Schmidt 1959; Kennicutt 1983), using different predictors of ISM phase masses. While the top left panel shows the K-S law from direct observations of SFR and M_{H_2} , the other panels use different indirect gas mass estimates.

Note that the slope, width, and offset of the best-fit relation can all be significantly affected by a different choice of gas mass indicator. For example, when adopting an estimate of M_{H_2} based on L_{500} , the K-S relation becomes steeper and tighter than the true relation. Also note the extent to which an individual galaxy can move above/below the K-S relation using different gas estimates. The different-colored points on Figure 10 demonstrate that $>+1\sigma$ outliers can become consistent with the relation (using M_{H_2} based on L_{500}) and

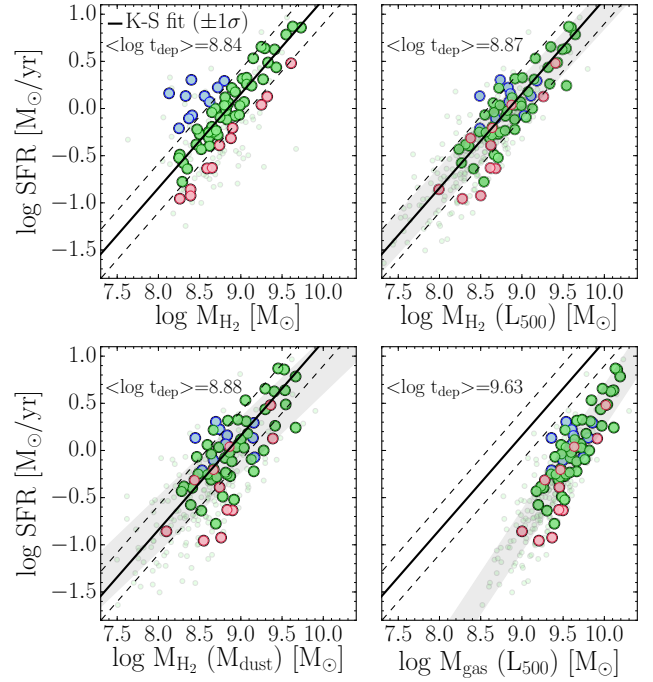


Figure 10. Integrated star formation law with different calibrations. Top left panel shows the true relation between the observed M_{H_2} and SFR, with the best-fit relationship (shown in all panels). Other panels plot observed SFR against various estimates of ISM phase masses, with analogous best-fits shown as grey-shaded regions. Galaxies are color-coded based on their position on, above, or below the relation. The full sample of HRS galaxies is included as faint points whenever available.

that $<-1\sigma$ outliers can move above the relation (using M_{H_2} based on M_{dust}).

The lower right panel of Figure 10 shows what can happen when using total M_{gas} instead of the star-forming M_{H_2} . This illustrates the impact of an incorrect assumption that the ISM is dominated by the molecular component when in fact it is mostly atomic. While this assumption is obviously inappropriate for the local HI-dominated galaxies in our sample, higher redshift galaxies have a wide range of $M_{\text{H}_2}/M_{\text{HI}}$ partitions and may not all be dominated by the molecular component (Cortese et al. 2017).

It can be dangerous to use these types of indirect estimates of gas masses to study the K-S relationship or other scaling relations. Any calibration of these gas mass estimates will be linked to the underlying physical properties of the ISM (e.g., atomic-to-molecular hydrogen ratio), and will not necessarily indicate variations in star formation efficiency. There are likely to be systematic effects lurking in these calibrations which will limit any attempt to derive a K-S relation using indirect gas mass predictions.

8 SUMMARY

Using a representative sample of $N=68$ nearby galaxies from the *Herschel* Reference Survey, we have calibrated a set of relationships between the masses of ISM phases and observable quantities (FIR and SFR). These predictive relationships can estimate ISM masses with $\sim 20\%$ accuracy and are

mutually self-consistent. However, our complete set of observations of all ISM phases show that these predictive relationships suffer from modest *systematic residual dependences on the molecular-to-atomic partition and other physical properties*. Any application of these relationships to predict gas masses from FIR/SFR observations requires an implicit assumption of the underlying $M_{\text{H}_2}/M_{\text{HI}}$ ratio. Incorrect assumptions about the dominant phase of the ISM can yield errors in gas mass predictions as large as 0.5 dex. Furthermore, using these indirect gas estimates to test the evolution of star formation laws or other scaling relations is potentially problematic, as these relations rely on those underlying scaling relations to successfully predict gas masses.

ACKNOWLEDGEMENTS

We thank Toby Brown and Katinka Geréb for helpful discussions, and the anonymous referee for their comments which have significantly improved this work and its statistical treatment of residual trends.

SJ, BC, and LC acknowledge support from the Australian Research Council's Discovery Project funding scheme (DP150101734). BC is the recipient of an Australian Research Council Future Fellowship (FT120100660). AG acknowledges support from the ICRAR Summer Studentship Programme during which this project was initiated.

This research has made use of NASA's Astrophysics Data System, and also the NASA/IPAC Extragalactic Database (NED), which is operated by the Jet Propulsion Laboratory, California Institute of Technology, under contract with the National Aeronautics and Space Administration. This research has also made use of the NASA/IPAC Infrared Science Archive, which is operated by the Jet Propulsion Laboratory, California Institute of Technology, under contract with the National Aeronautics and Space Administration. Finally, this research has made extensive use of the invaluable Tool for OPERations on Catalogues And Tables (TOPCAT², Taylor 2005).

REFERENCES

- Abazajian, K. N., Adelman-McCarthy, J. K., Agüeros, M. A., et al. 2009, *ApJS*, 182, 543-558
- Accurso, G., Saintonge, A., Catinella, B., et al. 2017, *MNRAS*, 470, 4750
- Alam, S., Albareti, F. D., Allende Prieto, C., et al. 2015, *ApJS*, 219, 12
- Aravena, M., Carilli, C. L., Salvato, M., et al. 2012, *MNRAS*, 426, 258
- Bauermeister, A., Blitz, L., Bolatto, A., et al. 2013, *ApJ*, 768, 132
- Berta, S., Lutz, D., Genzel, R., Förster-Schreiber, N. M., & Tacconi, L. J. 2016, *A&A*, 587, A73
- Bialy, S., Burkhart, B., & Sternberg, A. 2017, arXiv:1703.08549
- Bigiel, F., Leroy, A., Walter, F., et al. 2008, *AJ*, 136, 2846
- Bolatto, A. D., Wolfire, M., & Leroy, A. K. 2013, *ARA&A*, 51, 207
- Boselli, A., Lequeux, J., & Gavazzi, G. 2002, *A&A*, 384, 33
- Boselli, A., Eales, S., Cortese, L., et al. 2010, *PASP*, 122, 261
- Boselli, A., Cortese, L., & Boquien, M. 2014, *A&A*, 564, A65
- Boselli, A., Fossati, M., Gavazzi, G., et al. 2015, *A&A*, 579, A102
- Bourne, N., Dunne, L., Maddox, S. J., et al. 2016, *MNRAS*, 462, 1714
- Carilli, C. L., & Walter, F. 2013, *ARA&A*, 51, 105
- Catinella, B., Schiminovich, D., Kauffmann, G., et al. 2010, *MNRAS*, 403, 683
- Catinella, B., & Cortese, L. 2015, *MNRAS*, 446, 3526
- Catinella, B., Schiminovich, D., Cortese, L., et al. 2013, *MNRAS*, 436, 34
- Catinella, B., et al. submitted
- Ciesla, L., Boselli, A., Smith, M. W. L., et al. 2012, *A&A*, 543, A161
- Ciesla, L., Boquien, M., Boselli, A., et al. 2014, *A&A*, 565, A128
- Cortese, L., Ciesla, L., Boselli, A., et al. 2012, *A&A*, 540, A52
- Cortese, L., Fritz, J., Bianchi, S., et al. 2014, *MNRAS*, 440, 942
- Cortese, L., Bekki, K., Boselli, A., et al. 2016, *MNRAS*, 459, 3574
- Cortese, L., Catinella, B., Janowiecki, S. 2017, accepted to *ApJL*, arXiv:1709.07933
- Cybulski, R., Yun, M. S., Erickson, N., et al. 2016, *MNRAS*, 459, 3287
- da Cunha, E., Eminian, C., Charlot, S., & Blaizot, J. 2010, *MNRAS*, 403, 1894
- Daddi, E., Bournaud, F., Walter, F., et al. 2010, *ApJ*, 713, 686
- Draine, B. T., Dale, D. A., Bendo, G., et al. 2007, *ApJ*, 663, 866
- Draine, B. T., & Li, A. 2007, *ApJ*, 657, 810
- Eales, S., Smith, M. W. L., Auld, R., et al. 2012, *ApJ*, 761, 168
- Fernández, X., Gim, H. B., van Gorkom, J. H., et al. 2016, *ApJ*, 824, L1
- Genzel, R., Tacconi, L. J., Lutz, D., et al. 2015, *ApJ*, 800, 20
- Glover, S. C. O., & Clark, P. C. 2012, *MNRAS*, 421, 9
- Goiz, D., Monaco, P., Granato, G. L., et al. 2017, *MNRAS*, 469, 3775
- Groves, B. A., Schinnerer, E., Leroy, A., et al. 2015, *ApJ*, 799, 96
- Haynes, M. P., & Giovanelli, R. 1984, *AJ*, 89, 758
- Hodge, J. A., Carilli, C. L., Walter, F., Daddi, E., & Riechers, D. 2013, *ApJ*, 776, 22
- Hughes, T. M., Cortese, L., Boselli, A., Gavazzi, G., & Davies, J. I. 2013, *A&A*, 550, A115
- Hughes, T. M., Ibar, E., Villanueva, V., et al. 2017, arXiv:1702.07350
- Janowiecki, S., Catinella, B., Cortese, L., et al. 2017, *MNRAS*, 466, 4795
- Kennicutt, R. C., Jr. 1983, *ApJ*, 272, 54
- Kennicutt, R. C., Jr. 1998, *ARA&A*, 36, 189
- Kewley, L. J., & Ellison, S. L. 2008, *ApJ*, 681, 1183-1204
- Krumholz, M. R., McKee, C. F., & Tumlinson, J. 2009, *ApJ*, 693, 216
- Leroy, A. K., Walter, F., Brinks, E., et al. 2008, *AJ*, 136, 2782
- Leroy, A. K., Walter, F., Bigiel, F., et al. 2009, *AJ*, 137, 4670
- Leroy, A. K., Bolatto, A., Gordon, K., et al. 2011, *ApJ*, 737, 12
- Madau, P., & Dickinson, M. 2014, *ARA&A*, 52, 415
- Magdis, G. E., Daddi, E., Béthermin, M., et al. 2012, *ApJ*, 760, 6
- McKee, C. F., & Ostriker, E. C. 2007, *ARA&A*, 45, 565
- Noeske, K. G., Weiner, B. J., Faber, S. M., et al. 2007, *ApJ*, 660, L43
- Oliver, S. J., Bock, J., Altieri, B., et al. 2012, *MNRAS*, 424, 1614
- Pettini, M., & Pagel, B. E. J. 2004, *MNRAS*, 348, L59
- Reddy, N. A., Erb, D. K., Pettini, M., Steidel, C. C., & Shapley, A. E. 2010, *ApJ*, 712, 1070
- Rémy-Ruyer, A., Madden, S. C., Galliano, F., et al. 2013, *A&A*, 557, A95
- Roberts, M. S. 1963, *ARA&A*, 1, 149
- Saintonge, A., Kauffmann, G., Kramer, C., et al. 2011a, *MNRAS*, 415, 32
- Saintonge, A., Kauffmann, G., Wang, J., et al. 2011b, *MNRAS*, 415, 61

² <http://www.starlink.ac.uk/topcat/>

- Saintonge, A., Catinella, B., Cortese, L., et al. 2016, MNRAS, 462, 1749
- Salim, S., Rich, R. M., Charlot, S., et al. 2007, ApJS, 173, 267
- Schinnerer, E., Groves, B., Sargent, M. T., et al. 2016, ApJ, 833, 112
- Schmidt, M. 1959, ApJ, 129, 243
- Scoville, N., Aussel, H., Brusa, M., et al. 2007, ApJS, 172, 1
- Scoville, N., Aussel, H., Sheth, K., et al. 2014, ApJ, 783, 84
- Scoville, N., Sheth, K., Aussel, H., et al. 2016, ApJ, 820, 83
- Scoville, N., Lee, N., Vanden Bout, P., et al. 2017, ApJ, 837, 150
- Strong, A. W., Bloemen, J. B. G. M., Dame, T. M., et al. 1988, A&A, 207, 1
- Tacconi, L. J., Neri, R., Genzel, R., et al. 2013, ApJ, 768, 74
- Taylor, M. B. 2005, Astronomical Data Analysis Software and Systems XIV, 347, 29
- Valiante, E., Smith, M. W. L., Eales, S., et al. 2016, MNRAS, 462, 3146
- Viero, M. P., Asboth, V., Roseboom, I. G., et al. 2014, ApJS, 210, 22
- Whitaker, K. E., van Dokkum, P. G., Brammer, G., & Franx, M. 2012, ApJ, 754, L29
- Whitaker, K. E., Franx, M., Leja, J., et al. 2014, ApJ, 795, 104
- Zibetti, S., Charlot, S., & Rix, H.-W. 2009, MNRAS, 400, 1181

APPENDIX A: CAVEATS TO DETECTING SYSTEMATIC TRENDS

We undertook a Monte Carlo (MC) analysis to more fully understand and interpret the nature of the residual systematic trends explored in this work. One of our main points is the importance of the $M_{\text{H}_2}/M_{\text{HI}}$ ratio in applying indirect predictions of cold gas masses. However, this MC analysis demonstrates that one must be cautious when exploring dependences on that ratio, as certain techniques will show apparent residual trends which are partially specious and misleading. To verify that our results are not affected by non-physical trends, we describe our MC approach and analysis below.

To simulate and test the relationships between L_{500} and cold gas masses, we start by generating a random distribution of L_{500} values ($N=10,000$) consistent with that of our sample. We use our relationship between L_{500} and M_{gas} to generate estimates for the total gas content, and add random noise to the estimates to match our observed dispersion of $\sigma=0.15$ dex. We next generate a distribution of $M_{\text{H}_2}/M_{\text{HI}}$ values which matches that of our sample, ranging from $\sim 3\%$ to $\sim 300\%$, and calculate M_{H_2} and M_{HI} for each value of M_{gas} using this ratio. The top two rows of Figure A1 show histograms of these quantities and the relationships with L_{500} , where grey points and red lines show our observations and green points and lines show the simulated MC data. Note that we only input the L_{500} - M_{gas} relation into this MC, and we naturally recover the observed slope, correlation strength, and scatter in the L_{500} - M_{HI} relation. However, the resulting MC version of the L_{500} - M_{H_2} relation does not agree as well with the observed relation, although the two distributions of points have significant overlap.

The bottom two rows of Figure A1 show two different techniques (i.e., quantities on the x-axes) for quantifying residual trends in our L_{500} -based predictions of M_{HI} and M_{H_2} . The left two panels show the same type of analysis as used in this work: the ratio of M_{HI} to its prediction is plotted against M_{H_2} , and vice versa for the M_{H_2} prediction ratio

against M_{HI} . In both cases, the slope of the MC residuals is similar to our observations, although our observed trend with $M_{\text{HI}}/M_{\text{HI}}(L_{500})$ is slightly larger than the MC value and the scatter about the $M_{\text{H}_2}/M_{\text{H}_2}(L_{500})$ residual is over twice as large as our observations.

The right two panels show a different approach to measure the residuals as a function of $M_{\text{H}_2}/M_{\text{HI}}$, which is expected to drive these trends. However, since M_{HI} (or M_{H_2}) appears on both axes, both the real and MC sample show enhanced trends as a function of $M_{\text{H}_2}/M_{\text{HI}}$. While not physical, this type of plot is useful when interpreting L_{500} -based predictions for galaxies with different molecular-to-atomic gas mass ratios. Nonetheless, *caution is advised when quantifying residual trends in M_{HI} predictions as a function of $M_{\text{H}_2}/M_{\text{HI}}$.*

The agreement of this MC analysis with our observations suggests that the strongest predictive power comes from the L_{500} - M_{gas} relationship. This MC analysis goes one step further and shows that any attempt to use L_{500} to predict M_{HI} or M_{H_2} alone will suffer from a systematic dependence on the (potentially unknown) $M_{\text{H}_2}/M_{\text{HI}}$ ratio. We also note that this MC analysis does not produce results which fully agree with our observations, indicating that further residual dependences on other physical properties (e.g., those discussed in Section 6.3) may also play a role in these relationships.

This paper has been typeset from a $\text{\TeX}/\text{\LaTeX}$ file prepared by the author.

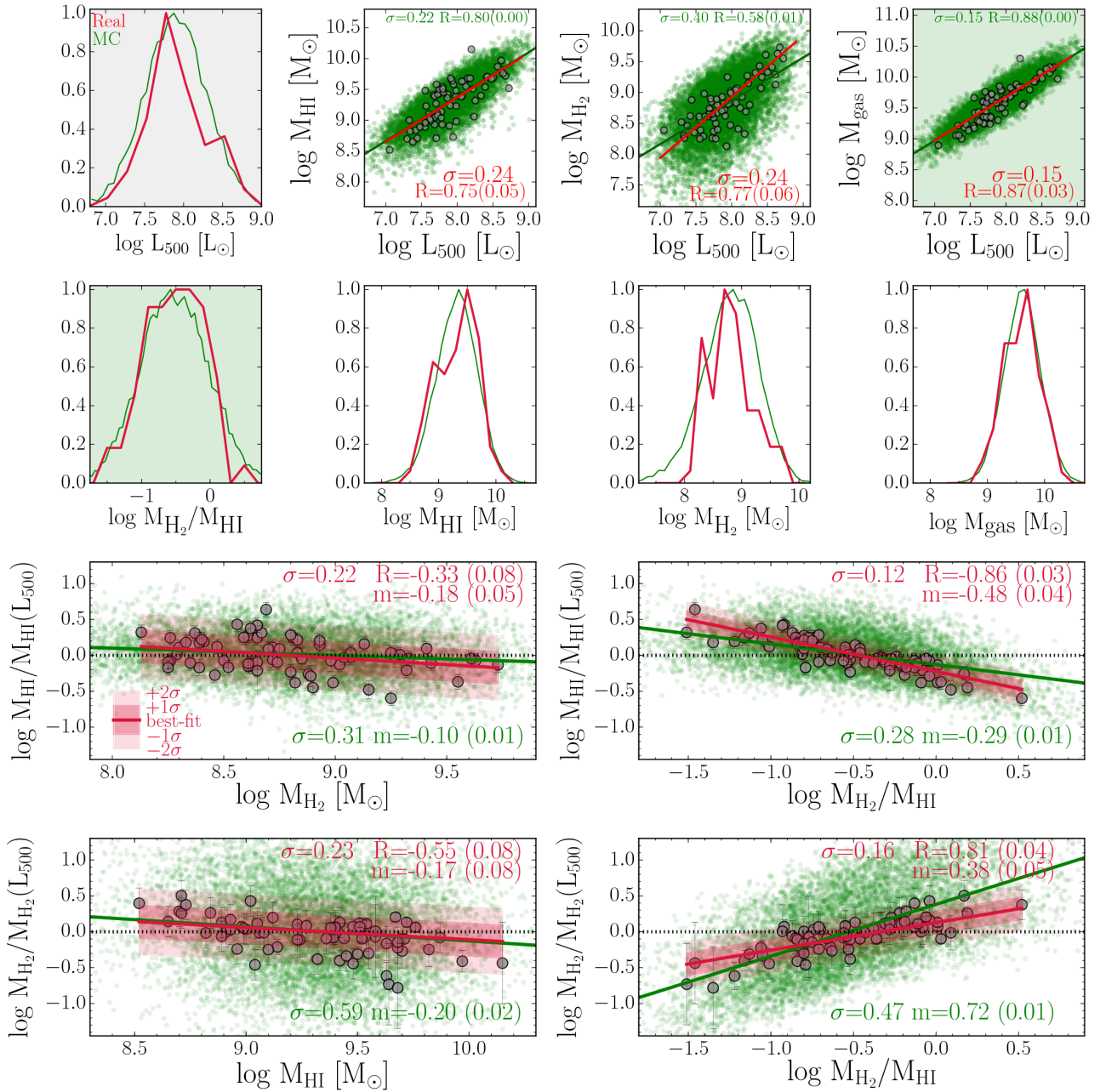


Figure A1. Full summary plots of our Monte Carlo for L_{500} -based predictions of cold gas masses. In all panels, grey points and red lines show data, histograms, and fits to our real observations; green points and lines show the simulated data.